

# Magnetocaloric effect and its electric-field regulation in $\text{CrI}_3$ /metal heterostructure

Weiwei He,<sup>†,¶</sup> Ziming Tang,<sup>†,¶</sup> Qihua Gong,<sup>\*,†,‡</sup> Min Yi,<sup>\*,†</sup> and Wanlin Guo<sup>†</sup>

<sup>†</sup>*State Key Laboratory of Mechanics and Control for Aerospace Structures & Key Lab for Intelligent Nano Materials and Devices of Ministry of Education & Institute for Frontier Science, Nanjing University of Aeronautics and Astronautics (NCAA), Nanjing 210016, China*

<sup>‡</sup>*MIT Key Laboratory of Aerospace Information Materials and Physics & College of Physics, Nanjing University of Aeronautics and Astronautics (NCAA), Nanjing 211106, China*

<sup>¶</sup>*Authors contributed equally.*

E-mail: [gongqihua@nuaa.edu.cn](mailto:gongqihua@nuaa.edu.cn); [yimin@nuaa.edu.cn](mailto:yimin@nuaa.edu.cn)

## Abstract

The extraordinary properties of a heterostructure by stacking atom-thick van der Waals (vdW) magnets have been extensively studied. However, the magnetocaloric effect (MCE) of heterostructures that are based on monolayer magnets remains to be explored. Herein, we deliberate MCE of vdW heterostructure composed of a monolayer  $\text{CrI}_3$  and metal atomic layers (Ag, Hf, Au, and Pb). It is revealed that heterostructure engineering by introducing metal substrate can improve MCE of  $\text{CrI}_3$ , particularly boosting relative cooling power to  $471.72 \mu\text{J m}^{-2}$  and adiabatic temperature change to 2.1 K at 5 T for  $\text{CrI}_3/\text{Hf}$ . This improved MCE is ascribed to the enhancement of magnetic moment and intralayer exchange coupling in  $\text{CrI}_3$  due to the  $\text{CrI}_3$ /metal heterointerface induced charge transfer. Electric field is further found to tune MCE of  $\text{CrI}_3$  in heterostructures and could shift the peak temperature by around 10 K in  $\text{CrI}_3/\text{Hf}$ , thus manipulating the working temperature window of MCE. The discovered

electric-field and substrate regulated MCE in CrI<sub>3</sub>/metal heterostructure opens new avenues for low-dimensional magnetic refrigeration.

**Keywords:** Magnetocaloric effect, Heterostructure, Monolayer magnets, Metal substrate, Electric field

## 1. INTRODUCTION

Magnetic cooling based on magnetocaloric effect (MCE) has emerged as a promising alternative to gaseous cooling with its ever-increasing energy consumption and greenhouse gas emissions.<sup>1-4</sup> As the inherited characteristics of magnetic materials, MCE is closely related to the magnetic properties and magnetization behavior under a magnetic field. The unpaired spins in magnetic materials are aligned when a magnetic field is applied, leading to a decrease in magnetic entropy and subsequent release of heat into the surroundings. Using MCE, it is possible to achieve target temperatures ranging from ultra-low to room temperature.<sup>5,6</sup> Up to date, the majority of literature on MCE has focused on bulk magnetocaloric materials<sup>7-10</sup> or thin films with nanometers to micrometers thickness,<sup>11-13</sup> restricting the application of magnetic refrigeration in compact and miniaturized nanodevices.

In recent years, two-dimensional (2D) van der Waals (vdW) magnets with a wide variety of unconventional properties, which differ from their bulk counterparts,<sup>14-19</sup> have drawn immense interest in fundamental research and device applications.<sup>20-24</sup> Layered vdW magnets are bonded to each other through weak vdW forces, allowing the easy separation of monolayers. For instance, in the monolayer CrI<sub>3</sub> that is fabricated by micromechanical exfoliation of bulk CrI<sub>3</sub> crystals, the magnetic anisotropy cancels out the thermal fluctuations at finite temperatures and the long-range magnetic order remains.<sup>14</sup> Therefore, the spontaneous magnetization in 2D magnets offers new perspectives for exploring MCE down to the monolayer limit.

The application and characterization of monolayer CrI<sub>3</sub> usually requires that it be stacked on top of a substrate rather than isolated.<sup>25-27</sup> Thus, vdW magnetic heterostructures with intrinsic magnetism and excellent stacking capability have attracted extensive research.<sup>28-33</sup> Diverse combination of heterostructures formed by CrI<sub>3</sub> is an effective approach toward achieving novel properties, such as thermal spin-filtering effect,<sup>34</sup> quantum anomalous Hall effect,<sup>35,36</sup> half-metallicity<sup>37-39</sup>, and enhanced magnetic properties.<sup>40-42</sup> The effect of various substrates on CrI<sub>3</sub> in terms of MCE, however, remains to be elucidated, which has stimulated our great interests in MCE of CrI<sub>3</sub> in hererostructures.

In the present work, we investigate MCE of CrI<sub>3</sub>/metal heterostructure and its electric-

field ( $E$ ) control. Four types of metals, i.e., Ag, Hf, Au, and Pb, are chosen to construct the heterostructures with monolayer  $\text{CrI}_3$ . First-principles calculations indicate that metal substrates significantly enhance the magnetic moment and nearest-neighbor exchange interaction of  $\text{CrI}_3$ , while they have different roles in magnetocrystalline energy (MAE). Atomistic spin simulations show that Curie temperature ( $T_C$ ) and saturation magnetization of  $\text{CrI}_3$  in heterostructures are boosted compared with the free-standing one. In addition, magnetocaloric thermodynamics confirms that heterostructure engineering improves MCE of monolayer  $\text{CrI}_3$ , which is further enhanced in  $\text{CrI}_3/\text{Hf}$  by applying a negative  $E$ . Our work not only demystifies tunable MCE in 2D magnets via substrates and  $E$ , but also opens new vistas for low-dimensional magnetically cooling devices.

## 2. RESULTS AND DISCUSSION

### 2.1 Magnetic properties and its electric-field tunability

Due to the interfacial interaction, 2D vdW magnets can change their magnetic properties upon contact with other materials. Based on thermodynamic stability assessment, Yang et al. investigated the magnetic properties of  $\text{CrI}_3$  with 3d transition-metal atoms (from Sc to Zn) absorbed on its surface.<sup>43</sup> In our work, four types of metal are selected (e.g., Ag, Hf, Au, Pb) to construct heterostructures with a favorable lattice match. Fig. 1(a) shows the atomic stacking in  $\text{CrI}_3/\text{Pb}$  heterostructure. The other three types of  $\text{CrI}_3/\text{metal}$  (Ag, Au, and Hf) heterostructure are presented in Fig. S1 (Supporting Information). It is noteworthy that  $\text{CrI}_3$  in heterostructures has fixed lattice parameters of monolayer  $\text{CrI}_3$ , allowing the metals to be compressed or stretched within an acceptable strain range around  $\pm 5\%$ . As illustrated in Fig. 1(a), we are able to investigate  $E$  controlled magnetic properties of  $\text{CrI}_3/\text{metal}$  heterostructures with the help of dipole layer method.

Magnetic properties of  $\text{CrI}_3$  are affected by metal substrate and  $E$ . As shown in Fig. 1(b)-(f), the impact of different metal substrates on  $\text{CrI}_3$  are dissimilar. The magnetic moment,  $J_1$ , and  $T_C$  of  $\text{CrI}_3$  absorbed upon four kinds of metal layers are increased when compared to those of monolayer  $\text{CrI}_3$ . In contrast, MAE of  $\text{CrI}_3$  is weakened by Ag and Pb substrates, while Au and Hf substrates improve it. The change of  $J_2$  shows a similar trend. Taking  $\text{CrI}_3/\text{Hf}$  heterostructure as an example, a detail analysis of the influence of metal substrate on the magnetic moment and MAE of  $\text{CrI}_3$  is presented. As can be seen from Fig. S2, the introduction of Hf intrigues the redistribution of electrons from spin-down channel to spin-up channel on the  $\text{CrI}_3$  side, thereby increasing the magnetic moment of Cr in Fig. 1(b). Considering that I atom (5p-element) has a much stronger spin-orbit coupling (SOC) effect

than Cr ( $3d$ -element),<sup>44</sup>  $p$ -orbital resolved MAE of I is analyzed in Fig. S3. The enhancement of matrix element differences ( $p_x, p_y$ ) compensates for the decrease of ( $p_x, p_z$ ), eventually improving MAE of CrI<sub>3</sub>/Hf in Fig. 1(c).

Magnetic performance of CrI<sub>3</sub>/metal heterostructures under  $E$  exhibit more diverse variations. Fig. 1(b) shows the effect of  $E$  on the magnetic moment of Cr. It can be seen that compared to monolayer CrI<sub>3</sub>, heterostructures not only achieve an increase in magnetic moment of Cr by promoting spin polarization through charge transfer, but also introduce the strong magneto-electric response that is neglectable in monolayer CrI<sub>3</sub>. Under a positive  $E$ , the magnetic moment of Cr slightly decreases when the strength of  $E$  increases. This could be explained by the charge redistribution that leads to a decrease of net charge in the spin-up channel.<sup>41,45</sup> Fig. S2 further shows the charge difference in CrI<sub>3</sub>/Hf heterostructure

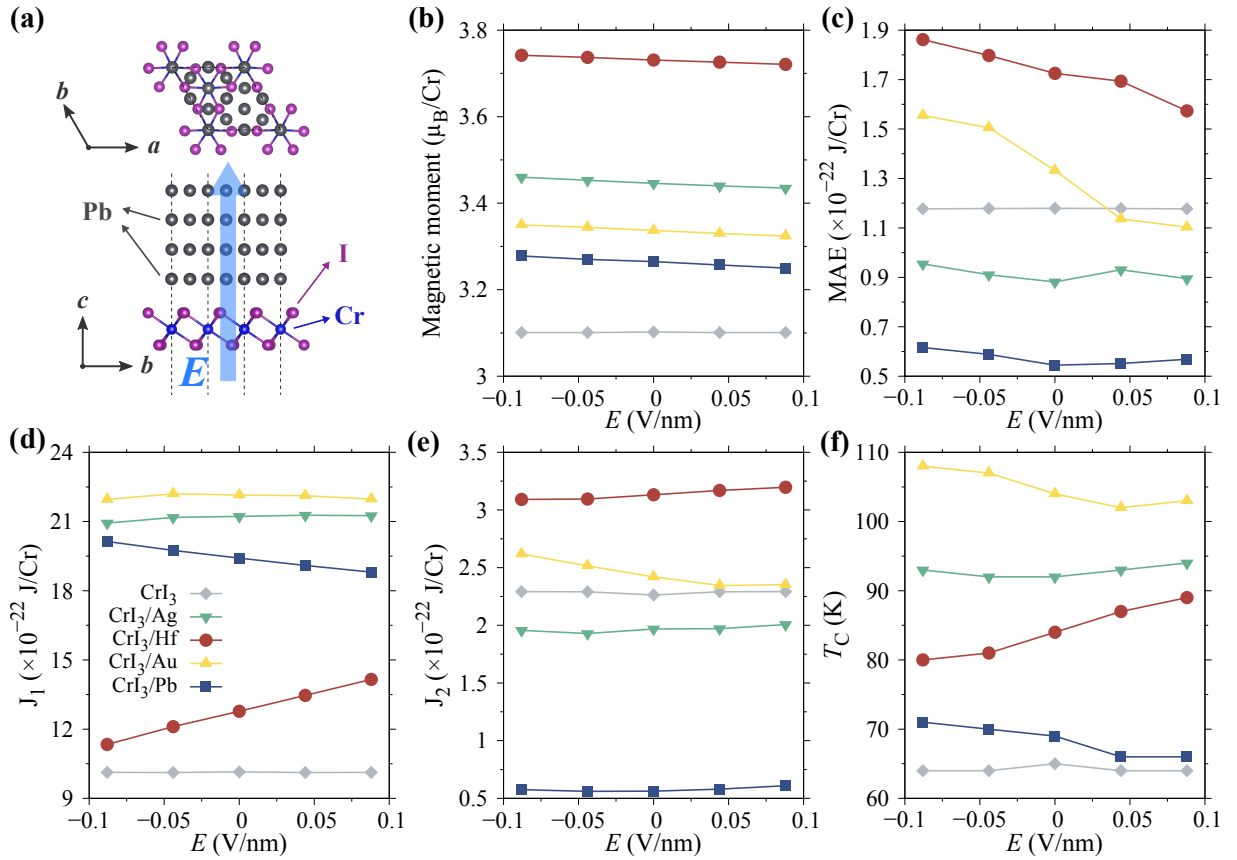


Figure 1: The atomic structure and magnetic properties of CrI<sub>3</sub> as a function of  $E$  in CrI<sub>3</sub>/metal vdW heterostructures. (a) Top and side views of CrI<sub>3</sub>/Pb(111) heterostructure. Dark grey, purple, and purplish-blue balls represent Pb, I, and Cr atoms, respectively. (b) Magnetic moment per Cr atom, (c) MAE, (d) and (e) magnetic exchange interaction parameters  $J_i$ , and (f)  $T_C$  of CrI<sub>3</sub> in monolayer and CrI<sub>3</sub>/metal heterostructures as a function of  $E$ .



under different  $E$ . MAE of  $\text{CrI}_3$  in  $\text{CrI}_3/\text{Hf}$  diminishes with the increasing  $E$ , as shown in Fig. 1(c). Similar to the  $\text{CrI}_3/\text{metal}$  heterostructure without  $E$ , the synergistic effect of matrix element differences ( $p_x, p_y$ ) and ( $p_x, p_z$ ) promotes the response of MAE to  $E$  (Fig. S3). Fig. 1(d) and 1(e) reveal the trends of ferromagnetic exchange interaction parameters  $J_1$  and  $J_2$  as a function of  $E$ . From our calculations, it is evident that when  $E$  is increased,  $J_1$  and  $J_2$  of  $\text{CrI}_3$  in  $\text{CrI}_3/\text{Hf}$  are enhanced, while  $J_1$  of  $\text{CrI}_3/\text{Pb}$  and  $J_2$  of  $\text{CrI}_3/\text{Au}$  are decreased. To explain the modulation of  $J_i$  by  $E$  and metal substrate, the energy differences between ferromagnetic (FM) and antiferromagnetic (AFM) states are presented in Fig. S4. Similar trends are also found in Fig. 1(f) :  $T_C$  of  $\text{CrI}_3$  in  $\text{CrI}_3/\text{Hf}$  increases by about 10 K as  $E$  is raised, whereas  $T_C$  of  $\text{CrI}_3$  adsorbed on Pb and Au decreases by 5 K.

## 2.2 Demagnetization behavior of $\text{CrI}_3$ in heterostructures

In our previous work,<sup>46</sup> we found that MCE indeed remains in various 2D magnets and can be remarkably tuned by strain. As a starting point for assessing MCE of  $\text{CrI}_3$  in heterostruc-

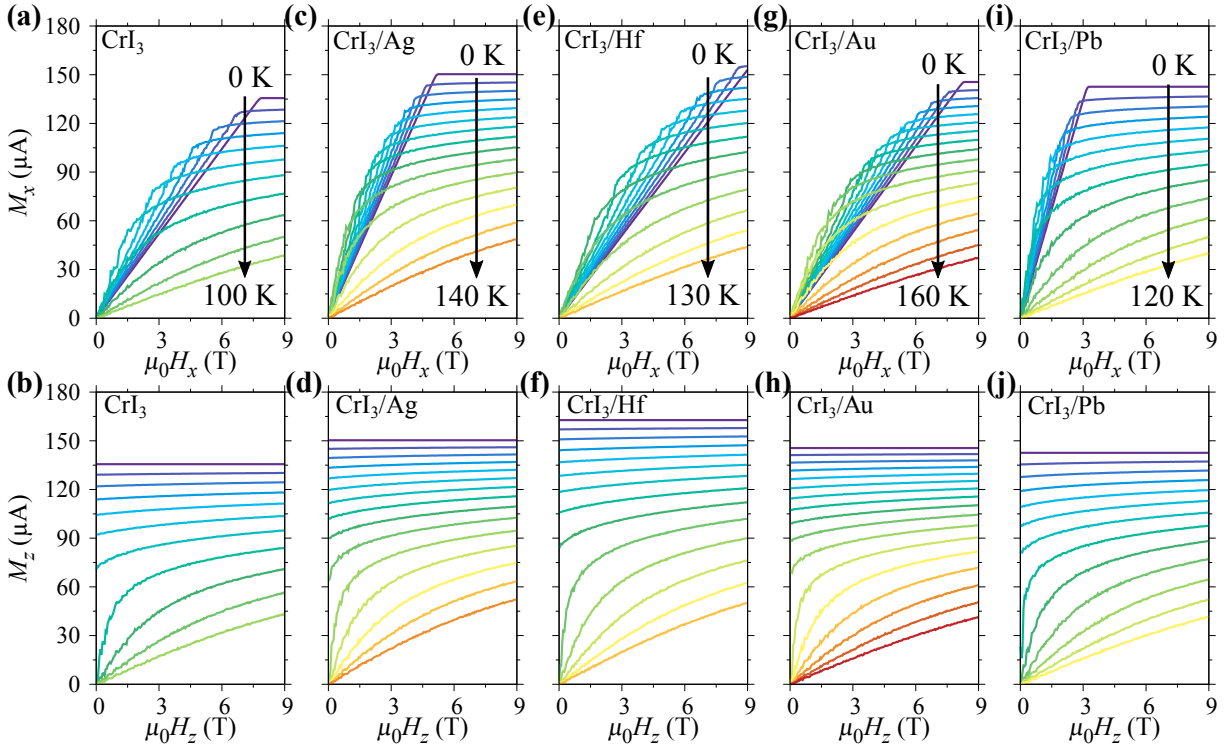


Figure 2: Isothermal magnetization curves of  $\text{CrI}_3$  in (a,b) monolayer  $\text{CrI}_3$ , (c,d)  $\text{CrI}_3/\text{Ag}$  heterostructure, (e,f)  $\text{CrI}_3/\text{Hf}$  heterostructure, (g,h)  $\text{CrI}_3/\text{Au}$  heterostructure, and (i,j)  $\text{CrI}_3/\text{Pb}$  heterostructure with magnetic field up to 9 T. The field directions are applied along in-plane for the top-row subfigures and out-of-plane for the bottom-row subfigures. The curves are displayed every 10 K.

tures, we first examine the demagnetization behavior of CrI<sub>3</sub> at different temperatures. Fig. 2 gives the isothermal magnetization curves in monolayer CrI<sub>3</sub> and heterostructures under in-plane and out-of-plane  $H$ . The magnetization vector of Cr atoms turns to the direction of applied field as  $H$  increases, and gradually becomes saturated under a high field. Moreover, saturation magnetization decreases with increasing temperature. Meanwhile, saturation magnetization of CrI<sub>3</sub> at 0 K should be proportional to the magnetic moment of Cr atom. Thus, CrI<sub>3</sub>/Hf heterostructure at the same temperature is expected to have the highest saturation magnetization according to Fig. 1(b).

Figure 2 also confirms the anisotropy of demagnetization behavior. The out-of-plane magnetic fields saturate magnetization curves much more easily than in-plane ones, owing to the out-of-plane MAE in Fig. 1(c). This anisotropic phenomenon has been explained at length in bulk CrI<sub>3</sub>,<sup>47,48</sup> and conclusions are also applicable to monolayers. When compared to monolayer CrI<sub>3</sub>, the magnetization curves of CrI<sub>3</sub> in CrI<sub>3</sub>/Ag and CrI<sub>3</sub>/Pb heterostructures tend to saturation at lower fields (Fig. 2(c) and(i)), while those of CrI<sub>3</sub> in CrI<sub>3</sub>/Hf and CrI<sub>3</sub>/Au heterostructures remain unsaturated under  $H$  up to 8 T (Fig. 2(e) and(d)). This is related to different effects of metal substrate on MAE of CrI<sub>3</sub>, which is similar to the trend in Fig. 1(c). In addition, magnetization curves in different heterostructures are distinguished at the same temperature. Compared with the magnetization curve of monolayer CrI<sub>3</sub> at 100 K, CrI<sub>3</sub> in CrI<sub>3</sub>/Au shows the same magnetization degree until 160 K. Magnetization curves of CrI<sub>3</sub> in CrI<sub>3</sub>/Hf at different  $E$  are supplemented in Fig. S5. The saturation magnetization at 0 K and the anisotropy under different  $E$  only change slightly under  $E$  modulation.

### 2.3 Magnetocaloric effect and its electric-field tunability

To explore the influence of metal substrates on MCE, maximum magnetic entropy change ( $-\Delta S_M^{\max}$ ), maximum adiabatic temperature change ( $\Delta T_{\text{ad}}^{\max}$ ), and relative cooling power (RCP) with a magnetic field of 5 T applied in different directions are shown in Fig. 3.  $-\Delta S_M^{\max}$ ,  $\Delta T_{\text{ad}}^{\max}$ , and RCP of monolayer CrI<sub>3</sub> in our work are calculated to be 13.48  $\mu\text{J m}^{-2} \text{K}$ , 1.89 K, and 404.35  $\mu\text{J m}^{-2}$ , respectively. The estimated results of monolayer CrI<sub>3</sub> are in good agreement with the experimental work of bulk counterpart,<sup>47</sup> whose  $-\Delta S_M^{\max}$  and  $\Delta T_{\text{ad}}^{\max}$  are measured as around 3.8  $\text{J kg}^{-1} \text{K}$  and 1.55 K under an out-of-plane magnetic field of 5 T. It also can be seen in Fig. 3 that metal substrates do improve MCE of CrI<sub>3</sub>, particularly in terms of increasing RCP. CrI<sub>3</sub> in all heterostructures achieves a higher RCP compared with monolayer CrI<sub>3</sub>, as shown in Fig. 3(c). Among them, RCP of CrI<sub>3</sub> in CrI<sub>3</sub>/Hf heterostructure is as high as 471.72  $\mu\text{J m}^{-2}$  at 5 T, suggesting there is more heat transferred between hot and cold reservoirs during a magnetic refrigeration cycle. In heterostructures, however,  $-\Delta S_M^{\max}$

of CrI<sub>3</sub> absorbed on four types of metal substrates does not surpass that of monolayer CrI<sub>3</sub> (Fig. 3(a)), mainly owing to the improved  $T_C$  of CrI<sub>3</sub>. More specifically, according to Eq 2, materials with superior  $-\Delta S_M^{\max}$  possess a comparatively larger magnetization and a relatively low  $T_C$ . The small increase in the magnetization cannot counteract the substantial improvement in  $T_C$  of CrI<sub>3</sub> in heterostructures, thus leading to a decrease in  $-\Delta S_M^{\max}$ . In contrast to  $-\Delta S_M^{\max}$ ,  $\Delta T_{\text{ad}}^{\max}$  reflects the enhancement of MCE by metal substrates. On account of the significantly improved magnetic moment and moderate  $T_C$ , Hf substrate can increase  $\Delta T_{\text{ad}}^{\max}$  of CrI<sub>3</sub> by 10.7% (up to 2.1 K) under an out-of-plane magnetic field, as shown in Fig. 3(b). The correlation between MCE and the applied field directions is also present in Fig. 3. It is clear that the difference between in-plane and out-of-plane MCE in CrI<sub>3</sub>/Hf heterostructure is larger than that in monolayer CrI<sub>3</sub>, while it is smaller in CrI<sub>3</sub>/Ag and CrI<sub>3</sub>/Pb heterostructures. The effect of substrates on anisotropic MCE in CrI<sub>3</sub> is also essentially attributed to the effect of substrates on MAE (Fig. 1(c)).

Figure 4(a) and (b) present the  $E$ -tunable MCE of CrI<sub>3</sub> in CrI<sub>3</sub>/Hf heterostructure under the in-plane and out-of-plane  $H$ . Our calculation results show that, the magnetocaloric performance of CrI<sub>3</sub> in CrI<sub>3</sub>/Hf heterostructure is further enhanced at a negative  $E$ , while the isothermal magnetic entropy change ( $-\Delta S_M$ ) decreased slightly at a positive  $E$  (Fig. 4(a)). This can be understood from Eq.2, which indicates that the partial derivative of magnetization with respect to temperature determines the entropy change. As shown in Fig. S5, a negative  $E$  induces the magnetization of CrI<sub>3</sub> in CrI<sub>3</sub>/Hf to be more sensitive to temperature changes than a positive  $E$ , resulting in higher  $-\Delta S_M^{\max}$  under the same  $H$ . A similar explanation can be used for  $\Delta T_{\text{ad}}^{\max}$  in Fig. 4(b). In addition, there is a consistent trend between the shift of peak temperature position in MCE curves and the adjustment of  $T_C$  regulated

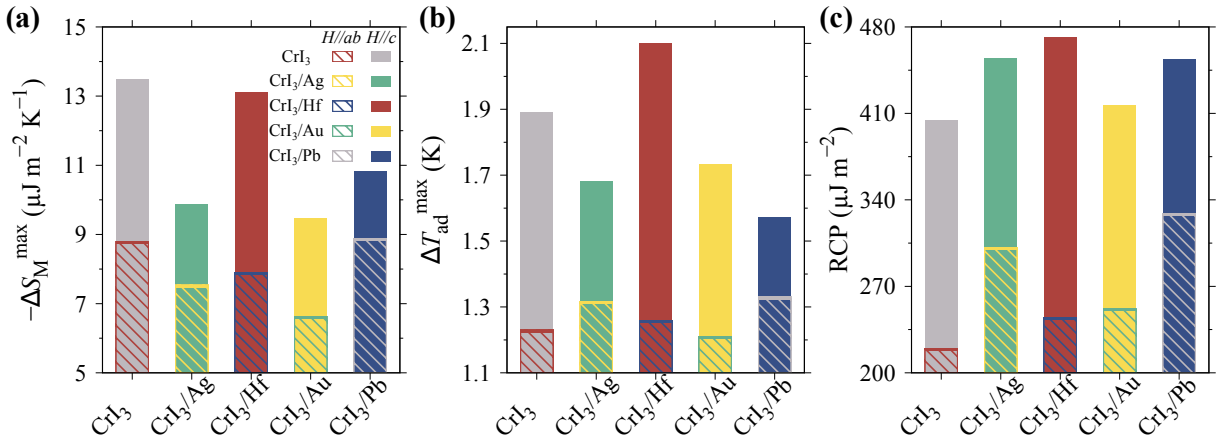


Figure 3: Influence of metal substrates on MCE of CrI<sub>3</sub> under a magnetic field of 5 T applied in different directions. (a) Maximum magnetic entropy change ( $-\Delta S_M^{\max}$ ), (b) maximum adiabatic temperature change ( $\Delta T_{\text{ad}}^{\max}$ ), and (c) relative cooling power (RCP).

by  $E$ , as shown in Fig. 4(a) and (b). By applying  $E$  to CrI<sub>3</sub>/Hf heterostructure, the peak temperature of  $-\Delta S_M$  and adiabatic temperature change ( $\Delta T_{ad}$ ) curves is shift up to 10 K, thereby extending the working temperature window of MCE for CrI<sub>3</sub>/metal heterostructures.  $-\Delta S_M$  and  $\Delta T_{ad}$  curves of CrI<sub>3</sub> in other heterostructures are given in Fig. S6 and Fig. S7, and these curves are almost unaffected by  $E$  modulation.

Schematic illustration of magnetic Carnot refrigeration cycle using CrI<sub>3</sub>/metal heterostructure under  $E$  is shown in Fig. 4(c). We propose an ideal assumption that when the cooled object touches a heterostructure under an applied periodic magnetic field, heat can be completely transferred outward from the cooled object. With an operating frequency of 1 Hz, the ideal specific cooling power (SCP) of CrI<sub>3</sub>/Hf heterostructure around 85 K is close to 1.3 nW cm<sup>-2</sup> at 5 T. Compared to monolayer CrI<sub>3</sub>,<sup>46</sup> CrI<sub>3</sub>/Hf heterostructure has an operating temperature increase of roughly 20 K owing to the metal substrate, and the operating temperature could be further shift up to 10 K by applying  $E$ .

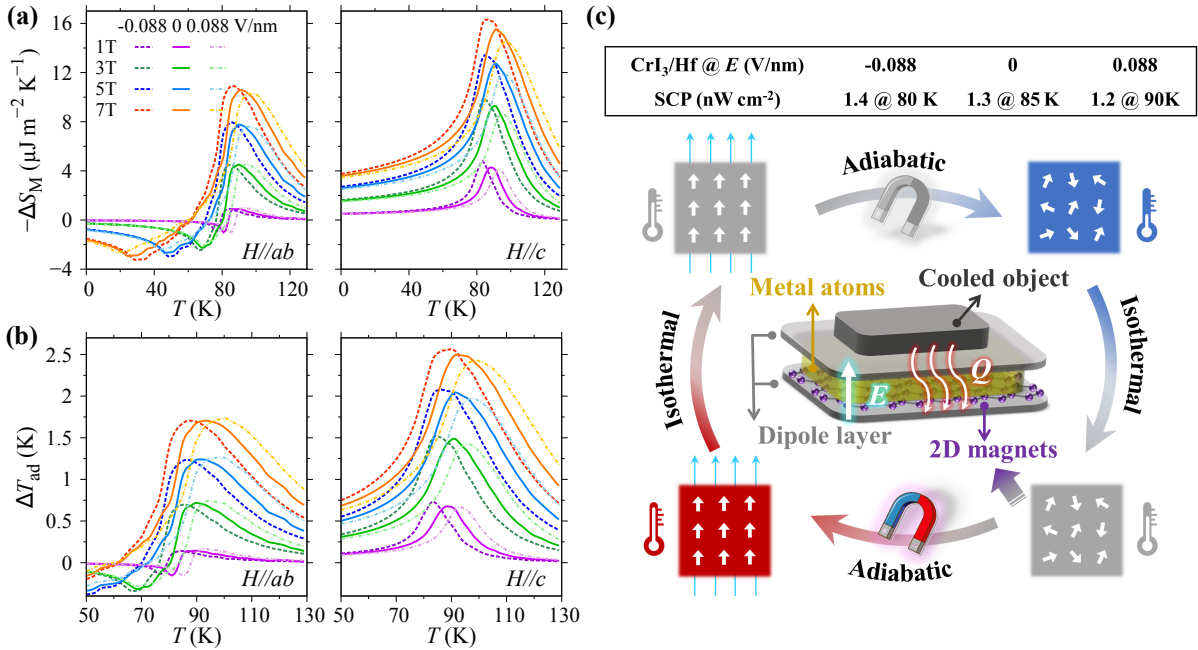


Figure 4: Electric-field-tunable MCE and its potential application in magnetic cooling.  $E$ -tunable (a) isothermal magnetic entropy change ( $-\Delta S_M$ ) and (b) adiabatic temperature change ( $\Delta T_{ad}$ ) vs  $T$  curves of CrI<sub>3</sub> in CrI<sub>3</sub>/Hf heterostructure. (c) Schematic illustration of Carnot refrigeration cycle using MCE of CrI<sub>3</sub>/metal heterostructure under  $E$ , in which specific cooling power (SCP) of CrI<sub>3</sub>/Hf heterostructure at 5 T is estimated.

### 3. CONCLUSIONS

In summary, MCE of monolayer CrI<sub>3</sub> absorbed on various metal substrates and its  $E$  modulation is comprehensively investigated using first-principles calculations, atomistic spin simulations, and magnetocaloric thermodynamics. Magnetic properties of CrI<sub>3</sub> are affected by metal substrates and exhibit more diverse variations under  $E$ , mainly owing to the charge transfer at the interface. Ag, Hf, Au, and Pb substrate are demonstrated to improve the magnetocaloric performance of CrI<sub>3</sub>, particularly with RCP and  $\Delta T_{\text{ad}}$  of CrI<sub>3</sub> in CrI<sub>3</sub>/Hf are increased to 471.72  $\mu\text{J m}^{-2}$  and 2.1 K at 5 T, respectively. Ag and Pb are found to weaken the MCE anisotropy, while Hf enhances it. Moreover, CrI<sub>3</sub> in CrI<sub>3</sub>/Hf with a negative  $E$  exhibits better magnetocaloric performance than that with a positive one. Through  $E$  modulation, the peak temperature of  $-\Delta S_{\text{M}}$  and  $\Delta T_{\text{ad}}$  curves in CrI<sub>3</sub>/Hf can be shift up to 10 K, allowing for widely tunable working temperature window of MCE. Our results on MCE of heterostructure formed by monolayer magnets and its  $E$  regulation provide an important basis for designing and building authentic low-dimensional magnetic refrigeration devices.

### 4. METHODOLOGY

The first-principles calculations within density functional theory are carried out to calculate the magnetic properties of monolayer CrI<sub>3</sub> absorbed on four types of metal substrates (Ag, Hf, Au, and Pb) by using *Vienna Ab initio Simulation Package* (VASP).<sup>49,50</sup> The exchange-correlation functional is treated with the the generalized gradient approximation (GGA) of the Perdew–Burke–Ernzerhof (PBE) form.<sup>51</sup> The CrI<sub>3</sub>/metal heterostructures are constructed by stacking four metallic layers onto a monolayer CrI<sub>3</sub> sheet. To avoid the interaction between neighboring slabs, the vacuum space along the  $z$ -axis is set to 35 Å.<sup>52</sup> A cutoff energy of 500 eV is utilized. The convergence criteria for energy and force in structure relaxation are  $10^{-5}$  eV and 0.01 eV/Å, respectively. The energy convergence is  $10^{-6}$  eV in self-consistent electronic calculations. The  $5 \times 5 \times 1$ ,  $11 \times 11 \times 1$ , and  $11 \times 11 \times 1$  Monkhorst–Pack  $k$ -mesh in the CrI<sub>3</sub>/Pb heterostructure ( $3 \times 3 \times 1$ ,  $5 \times 5 \times 1$ , and  $5 \times 5 \times 1$  in other heterostructures that contain more atoms) are adopted in the ionic optimization, electronic optimization, and MAE calculation, respectively.<sup>53</sup> The MAE is obtained by calculating the energy differences between the spin quantization axes whose directions are aligned with different crystallographic axes. In order to calculate the MAE, SOC is considered.<sup>54</sup> The magnetic exchange parameters are determined by substituting the magnetic configuration

energies into the classic spin Hamiltonian<sup>55</sup>

$$H = E_0 - \frac{1}{2}J_1 \sum_N \mathbf{s}_i \cdot \mathbf{s}_j - \frac{1}{2}J_2 \sum_{NN} \mathbf{s}_i \cdot \mathbf{s}_j, \quad (1)$$

where  $E_0$  is the energy without spin contribution,  $\mathbf{s}_i$  represents the unit vector of the atomistic spin direction at atom  $i$ .  $J_1$  and  $J_2$  denote the nearest-neighbour (NN) and next-NN exchange interaction parameters, respectively.

After obtaining the magnetic exchange parameters from first-principles calculations,  $T_C$  and temperature-dependent magnetization can be determined by the atomic spin model that has been numerically implemented in VAMPIRE.<sup>56-58</sup> The demagnetization field caused by the atomistic spins themselves is also considered. The figures of merit for MCE are generally described by  $\Delta S_M$  and  $\Delta T_{ad}$  upon a variation of magnetic field ( $H$ ). Based on the classical thermodynamics and the Maxwell relation,  $\Delta S_M$  is given by<sup>59,60</sup>

$$\Delta S_M = \int_0^H \left( \frac{\partial S}{\partial H} \right)_T dH = \mu_0 \int_0^H \left( \frac{\partial M}{\partial T} \right)_H dH, \quad (2)$$

where  $S$  and  $M$  refer to entropy and magnetization, respectively.  $\mu_0$  is vacuum permeability. Normally, MCE is characterized by  $-\Delta S_M$ , given that the degree of disorder in the magnetic moment decreases with increasing  $H$ .  $\Delta T_{ad}$  can be similarly calculated as

$$\begin{aligned} \Delta T_{ad} &= -\mu_0 \int_0^H \frac{T}{\rho c_p} \left( \frac{\partial S}{\partial H} \right)_T dH \\ &= -\mu_0 \int_0^H \frac{T}{\rho c_p} \left( \frac{\partial M}{\partial T} \right)_H dH, \end{aligned} \quad (3)$$

where  $\rho$  and  $c_p$  are density and specific heat capacity of monolayer  $\text{CrI}_3$ , respectively. RCP as another descriptor for MCE is used to characterize the heat transfer across reservoirs and reveal the potential MCE in magnets, which is calculated as

$$\text{RCP} = |\Delta S_M^{\max}| \times \delta T_{\text{FWHM}}, \quad (4)$$

where the  $\delta T_{\text{FWHM}}$  means the full width at half maximum of the  $-\Delta S_M$  vs  $T$  curve.

## Supporting Information

Top and side views of  $\text{CrI}_3/\text{metal}$  vdW heterostructures; Spin-dependent plane integrated charge density difference along  $c/z$  direction; The  $p$ -orbital resolved MAE of I atom in

CrI<sub>3</sub>; Energy difference between FM and AFM configurations of CrI<sub>3</sub> in CrI<sub>3</sub>/metal vdW heterostructures; Isothermal demagnetization curves of CrI<sub>3</sub> in CrI<sub>3</sub>/Hf heterostructure under different  $E$ ; Electric-field-tunable  $-\Delta S_M$  vs  $T$  curves for CrI<sub>3</sub>/metal heterostructures; Electric-field-tunable  $\Delta T_{ad}$  vs  $T$  curves for CrI<sub>3</sub>/metal heterostructures.

## Acknowledgment

The authors acknowledge the support from the National Natural Science Foundation of China (12272173, 11902150), the National Overseas Thousand Youth Talents Program, the Research Fund of State Key Laboratory of Mechanics and Control of Mechanical Structures (MCMS-I-0419G01 and MCMS-I-0421K01), a project Funded by the Priority Academic Program Development of Jiangsu Higher Education Institutions, and the Interdisciplinary Innovation Fund for Doctoral Students of Nanjing University of Aeronautics and Astronautics (KXKCXJJ202306). This work is partially supported by High Performance Computing Platform of Nanjing University of Aeronautics and Astronautics. Simulations were also performed on Hefei advanced computing center.

## References

- (1) Gutfleisch, O.; Willard, M. A.; Brück, E.; Chen, C. H.; Sankar, S. G.; Liu, J. P. Magnetic materials and devices for the 21st century: Stronger, lighter, and more energy efficient. *Advanced Materials* **2011**, *23*, 821–842.
- (2) Gottschall, T.; Skokov, K. P.; Fries, M.; Taubel, A.; Radulov, I.; Scheibel, F.; Benke, D.; Riegg, S.; Gutfleisch, O. Making a cool choice: The materials library of magnetic refrigeration. *Advanced Energy Materials* **2019**, *9*, 1901322.
- (3) Kitanovski, A.; Kitanovski, A. Energy applications of magnetocaloric materials. *Advanced Energy Materials* **2020**, *10*, 1903741.
- (4) Hou, H.; Qian, S.; Takeuchi, I. Materials, physics and systems for multicaloric cooling. *Nature Reviews Materials* **2022**, *7*, 633–652.
- (5) Hashimoto, T.; Numasawa, T.; Shino, M.; Okada, T. Magnetic refrigeration in the temperature range from 10 K to room temperature: The ferromagnetic refrigerants. *Cryogenics* **1981**, *21*, 647–653.

- (6) Zarkevich, N. A.; Zverev, V. I. Viable materials with a giant magnetocaloric effect. *Crystals* **2020**, *10*, 815.
- (7) Pecharsky, V. K.; Gschneidner, K. A. Giant Magnetocaloric Effect in  $\text{Gd}_5(\text{Si}_2\text{Ge}_2)$ . *Physical Review Letters* **1997**, *78*, 4494.
- (8) Luo, Q.; Zhao, D. Q.; Pan, M. X.; Wang, W. H. Magnetocaloric effect in Gd-based bulk metallic glasses. *Applied Physics Letters* **2006**, *89*, 081914.
- (9) Zhang, X. X.; Tejada, J.; Xin, Y.; Sun, G. F.; Wong, K. W.; Bohigas, X. Magnetocaloric effect in  $\text{La}_{0.67}\text{Ca}_{0.33}\text{MnO}_\delta$  and  $\text{La}_{0.60}\text{Y}_{0.07}\text{Ca}_{0.33}\text{MnO}_\delta$  bulk materials. *Applied Physics Letters* **2010**, *69*, 3596.
- (10) Franco, V.; Blázquez, J.; Ipus, J.; Law, J.; Moreno-Ramírez, L.; Conde, A. Magnetocaloric effect: From materials research to refrigeration devices. *Progress in Materials Science* **2018**, *93*, 112–232.
- (11) Moya, X.; Hueso, L. E.; Maccherozzi, F.; Tovstolytkin, A. I.; Podyalovskii, D. I.; Ducati, C.; Phillips, L. C.; Ghidini, M.; Hovorka, O.; Berger, A.; Vickers, M. E.; Defay, E.; Dhesi, S. S.; Mathur, N. D. Giant and reversible extrinsic magnetocaloric effects in  $\text{La}_{0.7}\text{Ca}_{0.3}\text{MnO}_3$  films due to strain. *Nature Materials* **2012**, *12*, 52–58.
- (12) Yüzüak, E.; Dincer, I.; Elerman, Y.; Auge, A.; Teichert, N.; Hütten, A. Inverse magnetocaloric effect of epitaxial Ni-Mn-Sn thin films. *Applied Physics Letters* **2013**, *103*, 222403.
- (13) Khovaylo, V. V.; Rodionova, V. V.; Shevyrtalov, S. N.; Novosad, V. Magnetocaloric effect in “reduced” dimensions: Thin films, ribbons, and microwires of Heusler alloys and related compounds. *Physica Status Solidi B* **2014**, *251*, 2104–2113.
- (14) Huang, B.; Clark, G.; Navarro-Moratalla, E.; Klein, D. R.; Cheng, R.; Seyler, K. L.; Zhong, D.; Schmidgall, E.; McGuire, M. A.; Cobden, D. H., et al. Layer-dependent ferromagnetism in a van der Waals crystal down to the monolayer limit. *Nature* **2017**, *546*, 270–273.
- (15) Gong, C.; Li, L.; Li, Z.; Ji, H.; Stern, A.; Xia, Y.; Cao, T.; Bao, W.; Wang, C.; Wang, Y., et al. Discovery of intrinsic ferromagnetism in two-dimensional van der Waals crystals. *Nature* **2017**, *546*, 265–269.



- (16) Bonilla, M.; Kolekar, S.; Ma, Y.; Diaz, H. C.; Kalappattil, V.; Das, R.; Eggers, T.; Gutierrez, H. R.; Phan, M. H.; Batzill, M. Strong room-temperature ferromagnetism in VSe<sub>2</sub> monolayers on van der Waals substrates. *Nature Nanotechnology* **2018**, *13*, 289–293.
- (17) Deng, Y.; Yu, Y.; Song, Y.; Zhang, J.; Wang, N. Z.; Sun, Z.; Yi, Y.; Wu, Y. Z.; Wu, S.; Zhu, J.; Wang, J.; Chen, X. H.; Zhang, Y. Gate-tunable room-temperature ferromagnetism in two-dimensional Fe<sub>3</sub>GeTe<sub>2</sub>. *Nature* **2018**, *563*, 94–99.
- (18) Yin, Y.; Yi, M.; Guo, W. High and anomalous thermal conductivity in monolayer MSi<sub>2</sub>Z<sub>4</sub> semiconductors. *ACS Applied Materials & Interfaces* **2021**, *13*, 45907–45915.
- (19) Yin, Y.; Gong, Q.; Yi, M.; Guo, W. Emerging versatile two-dimensional MoSi<sub>2</sub>N<sub>4</sub> family. *Advanced Functional Materials* **2022**, 2214050.
- (20) Li, H.; Ruan, S.; Zeng, Y. J. Intrinsic van der Waals magnetic materials from bulk to the 2D limit: New frontiers of spintronics. *Advanced Materials* **2019**, *31*, 1900065.
- (21) Hou, X.; Chen, H.; Zhang, Z.; Wang, S.; Zhou, P. 2D atomic crystals: A promising solution for next-generation data storage. *Advanced Electronic Materials* **2019**, *5*, 1800944.
- (22) Wang, H.; Qi, J.; Qian, X. Electrically tunable high Curie temperature two-dimensional ferromagnetism in van der Waals layered crystals. *Applied Physics Letters* **2020**, *117*, 083102.
- (23) Xue, M.; He, W.; Gong, Q.; Yi, M.; Guo, W. Nonlinear elasticity and strain-tunable magnetocalorics of antiferromagnetic monolayer MnPS<sub>3</sub>. *Extreme Mechanics Letters* **2022**, *57*, 101900.
- (24) Tang, Z. M.; Gong, Q.; Yi, M.-Y. Spin-selective contact type and strong Fermi level pinning at CrI<sub>3</sub>/metal interface. *Materials Today Nano* **2023**, *22*, 100309.
- (25) Li, T.; Jiang, S.; Sivadas, N.; Wang, Z.; Xu, Y.; Weber, D.; Goldberger, J. E.; Watanabe, K.; Taniguchi, T.; Fennie, C. J.; Fai Mak, K.; Shan, J. Pressure-controlled interlayer magnetism in atomically thin CrI<sub>3</sub>. *Nature Materials* **2019**, *18*, 1303–1308.
- (26) Ubrig, N.; Wang, Z.; Teyssier, J.; Taniguchi, T.; Watanabe, K.; Giannini, E.; Morpurgo, A. F.; Gibertini, M. Low-temperature monoclinic layer stacking in atomically thin CrI<sub>3</sub> crystals. *2D Materials* **2019**, *7*, 015007.

- (27) Guo, X. et al. Structural monoclinicity and its coupling to layered magnetism in few-layer CrI<sub>3</sub>. *ACS Nano* **2021**, *15*, 10444–10450.
- (28) Zhang, J.; Zhao, B.; Zhou, T.; Xue, Y.; Ma, C.; Yang, Z. Strong magnetization and Chern insulators in compressed graphene/CrI<sub>3</sub> van der Waals heterostructures. *Physical Review B* **2018**, *97*, 085401.
- (29) Song, T.; Cai, X.; Tu, M. W. Y.; Zhang, X.; Huang, B.; Wilson, N. P.; Seyler, K. L.; Zhu, L.; Taniguchi, T.; Watanabe, K.; McGuire, M. A.; Cobden, D. H.; Xiao, D.; Yao, W.; Xu, X. Giant tunneling magnetoresistance in spin-filter van der Waals heterostructures. *Science* **2018**, *360*, 1214–1218.
- (30) Gibertini, M.; Koperski, M.; Morpurgo, A. F.; Novoselov, K. S. Magnetic 2D materials and heterostructures. *Nature Nanotechnology* **2019**, *14*, 408–419.
- (31) Li, H.; Xu, Y. K.; Cheng, Z. P.; He, B. G.; Zhang, W. B. Spin-dependent Schottky barriers and vacancy-induced spin-selective ohmic contacts in magnetic vdW heterostructures. *Physical Chemistry Chemical Physics* **2020**, *22*, 9460–9466.
- (32) Gong, Q.; Yi, M.; Xu, B. X. Electric field induced magnetization reversal in magnet/insulator nanoheterostructure. *International Journal of Smart and Nano Materials* **2020**, *11*, 298–309.
- (33) Yao, Y.; Zhan, X.; Sendeku, M. G.; Yu, P.; Dajan, F. T.; Li, N.; Wang, J.; Zhu, C.; Wang, F.; Wang, Z.; He, J. Recent progress on emergent two-dimensional magnets and heterostructures. *Nanotechnology* **2021**, *32*, 472001.
- (34) Tan, X.; Ding, L.; Du, G. F.; Fu, H. H. Spin caloritronics in two-dimensional CrI<sub>3</sub>/NiCl<sub>2</sub> van der Waals heterostructures. *Physical Review B* **2021**, *103*, 115415.
- (35) Petrov, E. K.; Silkin, I. V.; Menshchikova, T. V.; Chulkov, E. V. Cr-containing ferromagnetic film–topological insulator heterostructures as promising materials for the quantum anomalous hall effect. *JETP Letters* **2019**, *109*, 121–125.
- (36) Gao, Y.; Li, H.; Zhu, W. Prediction of quantum anomalous Hall effect in CrI<sub>3</sub>/ScCl<sub>2</sub> bilayer heterostructure. *Chinese Physics B* **2022**, *31*, 107304.
- (37) Zhao, Y.; Zhang, J. J.; Yuan, S.; Chen, Z. Nonvolatile electrical control and heterointerface-induced half-metallicity of 2D ferromagnets. *Advanced Functional Materials* **2019**, *29*, 1901420.

- (38) Chakraborty, S.; Ravikumar, A. Substrate induced electronic phase transitions of CrI<sub>3</sub> based van der Waals heterostructures. *Scientific Reports* **2021**, *11*, 198.
- (39) Wang, G.; Qin, W.; Wang, S.; Teketel, B. S.; Yu, W.; Luo, T.; Xu, B.; Lin, B. CrI<sub>3</sub>/Y<sub>2</sub>CH<sub>2</sub>:Heterointerface-induced stable half-metallicity of two-dimensional CrI<sub>3</sub> monolayer ferromagnets. *ACS Applied Materials and Interfaces* **2021**, *13*, 16694–16703.
- (40) Chen, S.; Huang, C.; Sun, H.; Ding, J.; Jena, P.; Kan, E. Boosting the Curie temperature of two-dimensional semiconducting CrI<sub>3</sub> monolayer through van der Waals heterostructures. *The Journal of Physical Chemistry C* **2019**, *123*, 17987–17993.
- (41) Hu, J. K.; Tan, J. X.; Wu, D.; Zhang, Z. H.; Fan, Z. Q. Exploring magnetic stability and valley splitting on CrI<sub>3</sub>/SiC van der Waals heterostructure. *Applied Surface Science* **2021**, *560*, 149858.
- (42) Yu, W.; Luo, W.; Zhang, X.; Wu, Y.; Jia, X.; Yang, X.; Cai, X.; Song, A.; Zhang, Z.; Zhang, W. B. Strain and electric field dependent spin polarization in two-dimensional arsenene/CrI<sub>3</sub> heterostructure. *Journal of Alloys and Compounds* **2022**, *912*, 165093.
- (43) Yang, Q.; Hu, X.; Shen, X.; Krasheninnikov, A. V.; Chen, Z.; Sun, L. Enhancing ferromagnetism and tuning electronic properties of CrI<sub>3</sub> monolayers by adsorption of transition-metal atoms. *ACS Applied Materials & Interfaces* **2021**, *13*, 21593–21601.
- (44) Jiang, P.; Li, L.; Liao, Z.; Zhao, Y. X.; Zhong, Z. Spin direction-controlled electronic band structure in two-dimensional ferromagnetic CrI<sub>3</sub>. *Nano Letters* **2018**, *18*, 3844–3849.
- (45) Liu, J.; Shi, M.; Lu, J.; Anantram, M. P. Analysis of electrical-field-dependent Dzyaloshinskii-Moriya interaction and magnetocrystalline anisotropy in a two-dimensional ferromagnetic monolayer. *Physical Review B* **2018**, *97*, 8–10.
- (46) He, W.; Yin, Y.; Gong, Q.; Evans, R. F.; Gutfleisch, O.; Xu, B.; Yi, M.; Guo, W. Giant magnetocaloric effect in magnets down to the monolayer limit. *arXiv preprint* **2023**,
- (47) Liu, Y.; Petrovic, C. Anisotropic magnetocaloric effect in single crystals of CrI<sub>3</sub>. *Physical Review B* **2018**, *97*, 174418.
- (48) Tran, H. B.; Momida, H.; ichiro Matsushita, Y.; Shirai, K.; Oguchi, T. Insight into anisotropic magnetocaloric effect of CrI<sub>3</sub>. *Acta Materialia* **2022**, *231*, 117851.

- (49) Kresse, G.; Furthmüller, J. Efficient iterative schemes for *ab initio* total-energy calculations using a plane-wave basis set. *Physical Review B* **1996**, *54*, 11169–11186.
- (50) Kresse, G.; Joubert, D. From ultrasoft pseudopotentials to the projector augmented-wave method. *Physical Review B* **1999**, *59*, 1758–1775.
- (51) Perdew, J. P.; Burke, K.; Ernzerhof, M. Generalized Gradient Approximation Made Simple. *Physical Review Letters* **1996**, *77*, 3865–3868.
- (52) Neugebauer, J.; Scheffler, M. Adsorbate-substrate and adsorbate-adsorbate interactions of Na and K adlayers on Al(111). *Physical Review B* **1992**, *46*, 16067–16080.
- (53) Monkhorst, H. J.; Pack, J. D. Special points for Brillouin-zone integrations. *Physical Review B* **1976**, *13*, 5188–5192.
- (54) Vaz, C. A. F.; Bland, J. A. C.; Lauhoff, G. Magnetism in ultrathin film structures. *Reports on Progress in Physics* **2008**, *71*, 056501.
- (55) Skubic, B.; Hellsvik, J.; Nordström, L.; Eriksson, O. A method for atomistic spin dynamics simulations: Implementation and examples. *Journal of Physics: Condensed Matter* **2008**, *20*, 315203.
- (56) Evans, R. F.; Fan, W. J.; Churemart, P.; Ostler, T. A.; Ellis, M. O.; Chantrell, R. W. Atomistic spin model simulations of magnetic nanomaterials. *Journal of Physics: Condensed Matter* **2014**, *26*, 103202.
- (57) Gong, Q.; Yi, M.; Evans, R. F.; Xu, B. X.; Gutfleisch, O. Calculating temperature-dependent properties of Nd<sub>2</sub>Fe<sub>14</sub>B permanent magnets by atomistic spin model simulations. *Physical Review B* **2019**, *99*, 214409.
- (58) Gong, Q.; Yi, M.; Xu, B. X. Multiscale simulations toward calculating coercivity of Nd-Fe-B permanent magnets at high temperatures. *Physical Review Materials* **2019**, *3*, 84406.
- (59) Pecharsky, V. K.; Gschneidner, K. A. Magnetocaloric effect from indirect measurements: Magnetization and heat capacity. *Journal of Applied Physics* **1999**, *86*, 565–575.
- (60) Gschneidner, K. A.; Pecharsky, V. K. Magnetocaloric materials. *Annual Review of Materials Science* **2000**, *30*, 387–429.

# Supplementary information

## Magnetocaloric effect and its electric-field regulation in $\text{CrI}_3$ /metal heterostructure

Weiwei He,<sup>†,¶</sup> Ziming Tang,<sup>†,¶</sup> Qihua Gong,<sup>\*,†,‡</sup> Min Yi,<sup>\*,†</sup> and Wanlin Guo<sup>†</sup>

<sup>†</sup>*State Key Laboratory of Mechanics and Control for Aerospace Structures & Key Lab for Intelligent Nano Materials and Devices of Ministry of Education & Institute for Frontier Science, Nanjing University of Aeronautics and Astronautics (NUAA), Nanjing 210016, China*

<sup>‡</sup>*MIIT Key Laboratory of Aerospace Information Materials and Physics & College of Physics, Nanjing University of Aeronautics and Astronautics (NUAA), Nanjing 211106, China*

<sup>¶</sup>*Authors contributed equally.*

E-mail: gongqihua@nuaa.edu.cn; yimin@nuaa.edu.cn

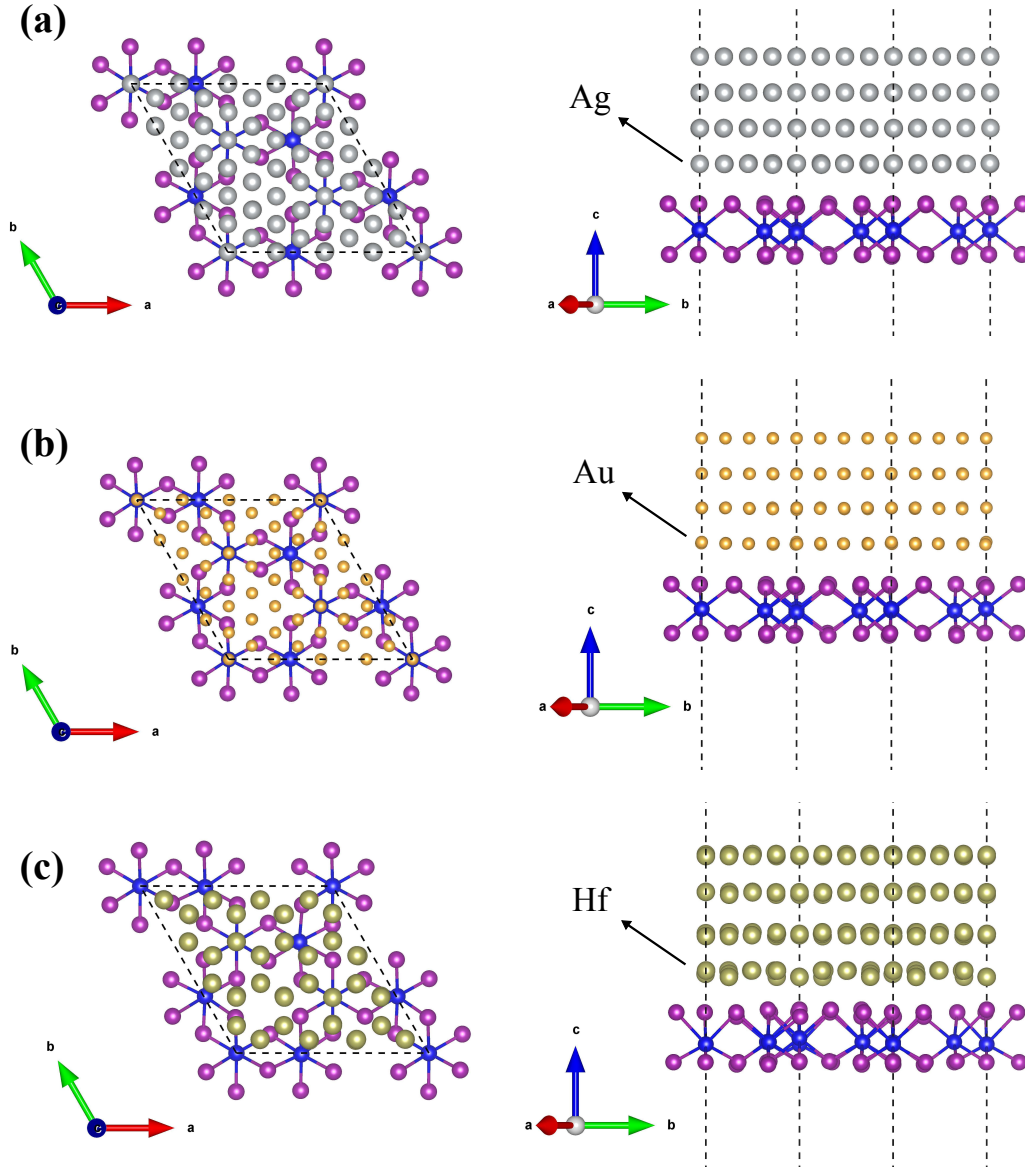


Fig. S1. Top and side views of  $\text{CrI}_3$ /metal vdW heterostructures: (a)  $\text{CrI}_3/\text{Ag}(111)$  configuration, (b)  $\text{CrI}_3/\text{Au}(111)$  configuration, and (c)  $\text{CrI}_3/\text{Hf}(001)$  configuration. The heterostructure of (a)  $\text{CrI}_3/\text{Ag}(111)$  and (b)  $\text{CrI}_3/\text{Au}(111)$  is built by placing a  $2 \times 2$  supercell of  $\text{Ag}(111)$  and  $\text{Au}(111)$  on  $\sqrt{3} \times \sqrt{3}$  unit cells of monolayer  $\text{CrI}_3$ . The heterostructure of (c)  $\text{CrI}_3/\text{Hf}(001)$  is built by placing a  $4 \times 4$  supercell of  $\text{Hf}(001)$  on  $\sqrt{3} \times \sqrt{3}$  unit cells of monolayer  $\text{CrI}_3$ . Silver, gold, greyish-green, purple, and purplish-blue balls represent Ag, Au, Hf, I, and Cr atoms, respectively.

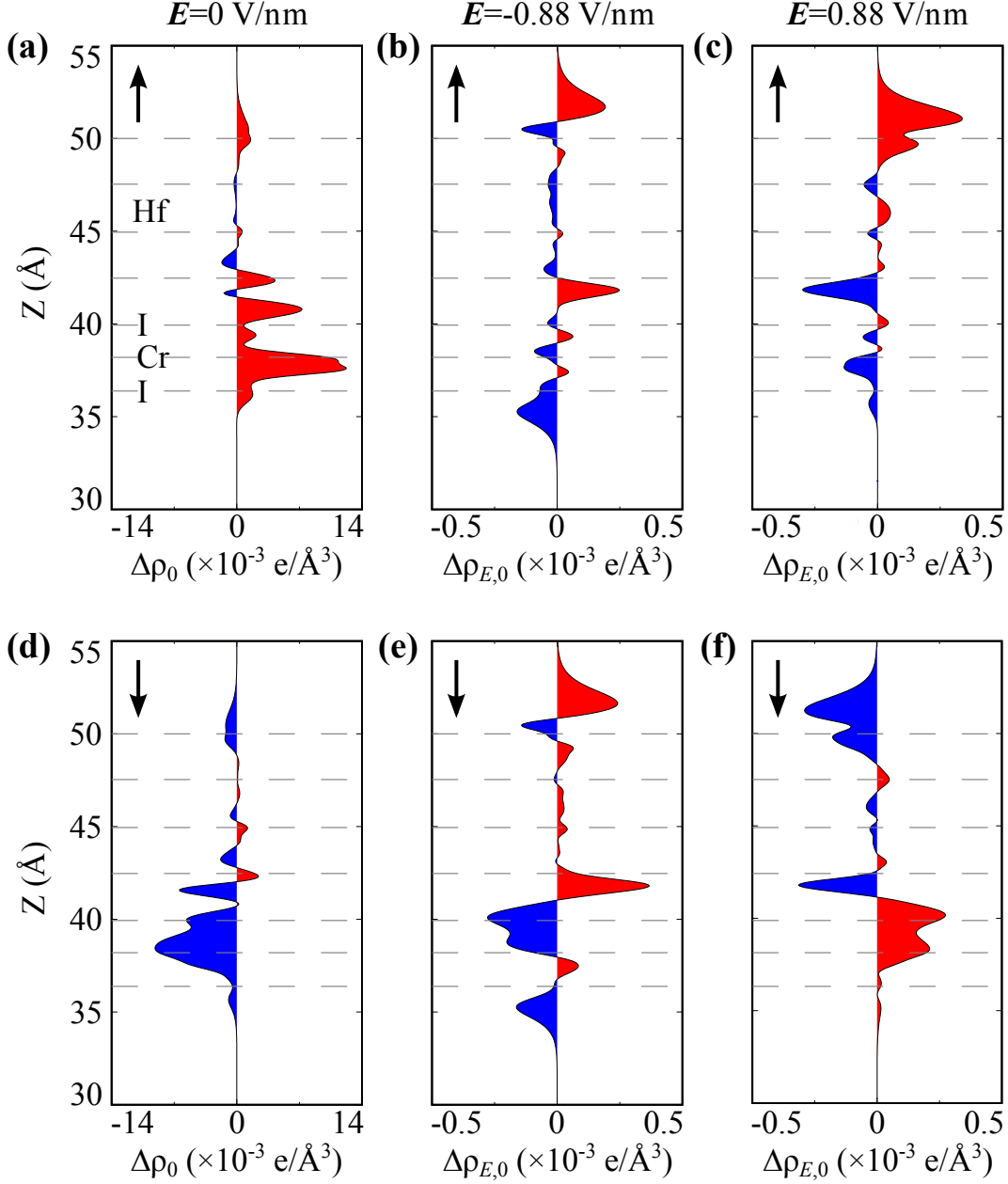


Fig. S2. Spin-dependent plane integrated charge density difference along  $c/z$  direction. (a), (d) Plane averaged charge density difference  $\Delta\rho_0$  of  $\text{CrI}_3/\text{Hf}$  without  $E$  in spin-up (spin-down) direction. Using  $\Delta\rho_0$  as a reference, the change  $\Delta\rho_{E,0}$  represents charge density difference of  $\text{CrI}_3/\text{Hf}$  under different  $E$ . (b), (e) Spin-up (spin-down) charge with  $E = -0.88 \text{ V/nm}$ . (c), (f) Spin-up (spin-down) charge with  $E = 0.88 \text{ V/nm}$ . After forming the  $\text{CrI}_3/\text{Hf}$  interface, there is an accumulation of electrons in  $\text{CrI}_3$  side in the spin-up channel while in the spin-down channel there exists a substantial depletion of electrons in (a) and (d). Such a charge redistribution leads to the stronger spin polarization, which unveils the reason that Hf substrate greatly improves the magnetic moment of Cr.<sup>1</sup> As depicted in (b) and (e), when the  $\text{CrI}_3/\text{Hf}$  is subjected to  $E = -0.88 \text{ V/nm}$ , although the charge in both spin channels exhibit depletion at  $\text{CrI}_3$ , the more losses of spin-down charge render a net increase of magnetic moment of Cr.

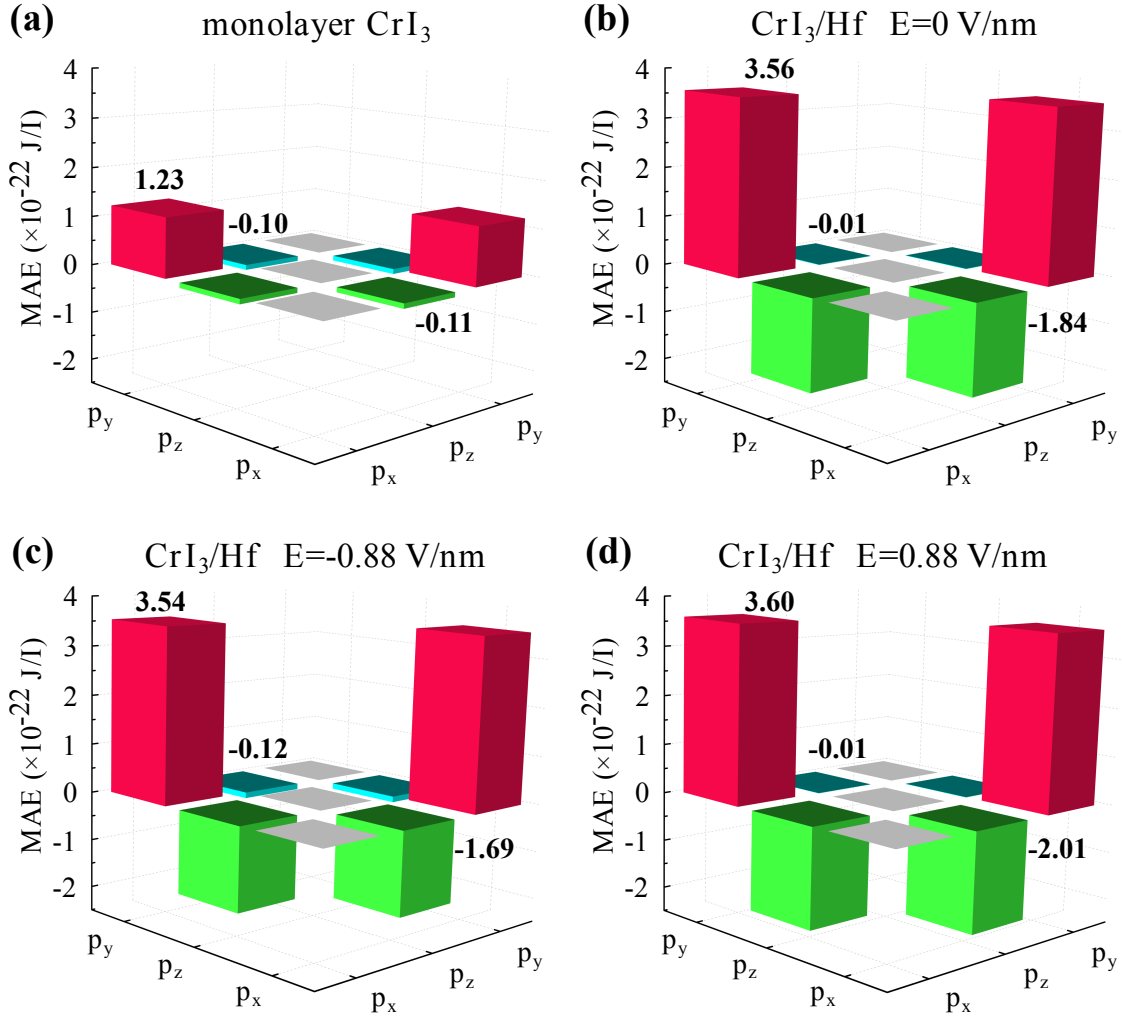


Fig. S3. The  $p$ -orbital resolved MAE of I atom in  $\text{CrI}_3$ : (a) monolayer  $\text{CrI}_3$ , (b)  $\text{CrI}_3$  in  $\text{CrI}_3/\text{Hf}$  heterostructure without  $E$ , (c)  $\text{CrI}_3$  in  $\text{CrI}_3/\text{Hf}$  heterostructure with  $E = -0.88$  V/nm, and (d)  $\text{CrI}_3$  in  $\text{CrI}_3/\text{Hf}$  heterostructure with  $E = 0.88$  V/nm. Compared to monolayer  $\text{CrI}_3$ , the large rise in the positive contribution of matrix element differences ( $p_x, p_y$ ) to perpendicular magnetic anisotropy in the  $\text{CrI}_3/\text{Hf}$  heterostructure compensates for the negative contribution from element differences ( $p_x, p_z$ ), resulting in an improvement in MAE. As the strength of  $E$  increases, there is a little increase in ( $p_x, p_y$ ), but the negative contribution of ( $p_x, p_z$ ) decreases more significantly, resulting in a decrease in MAE.



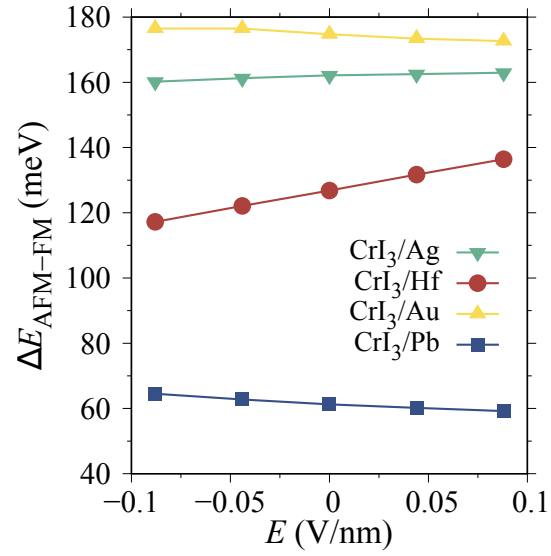


Fig. S4. Energy difference between FM and AFM configurations ( $\Delta E_{\text{FM-AFM}}$ ) of CrI<sub>3</sub> as a function of  $E$  in CrI<sub>3</sub>/metal vdW heterostructures.

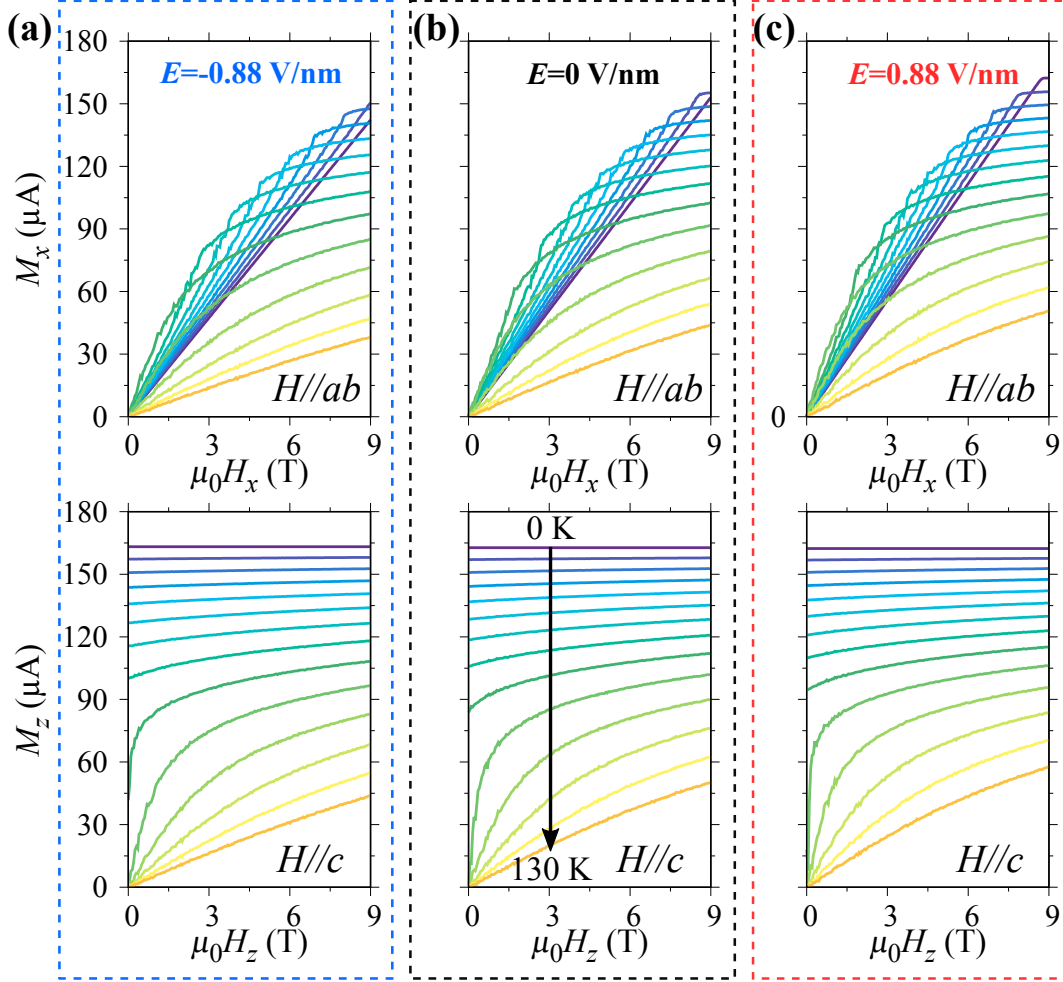


Fig. S5. Isothermal demagnetization curves of  $\text{CrI}_3$  in  $\text{CrI}_3/\text{Hf}$  heterostructure under a field up to 9 T: (a)  $E = -0.88 \text{ V/nm}$ , (b)  $E = 0 \text{ V/nm}$ , and (c)  $E = 0.88 \text{ V/nm}$ . The magnetic field direction is applied along the in-plane (top-row subfigures) and out-of-plane (bottom-row subfigures). The curves are displayed every 10 K.

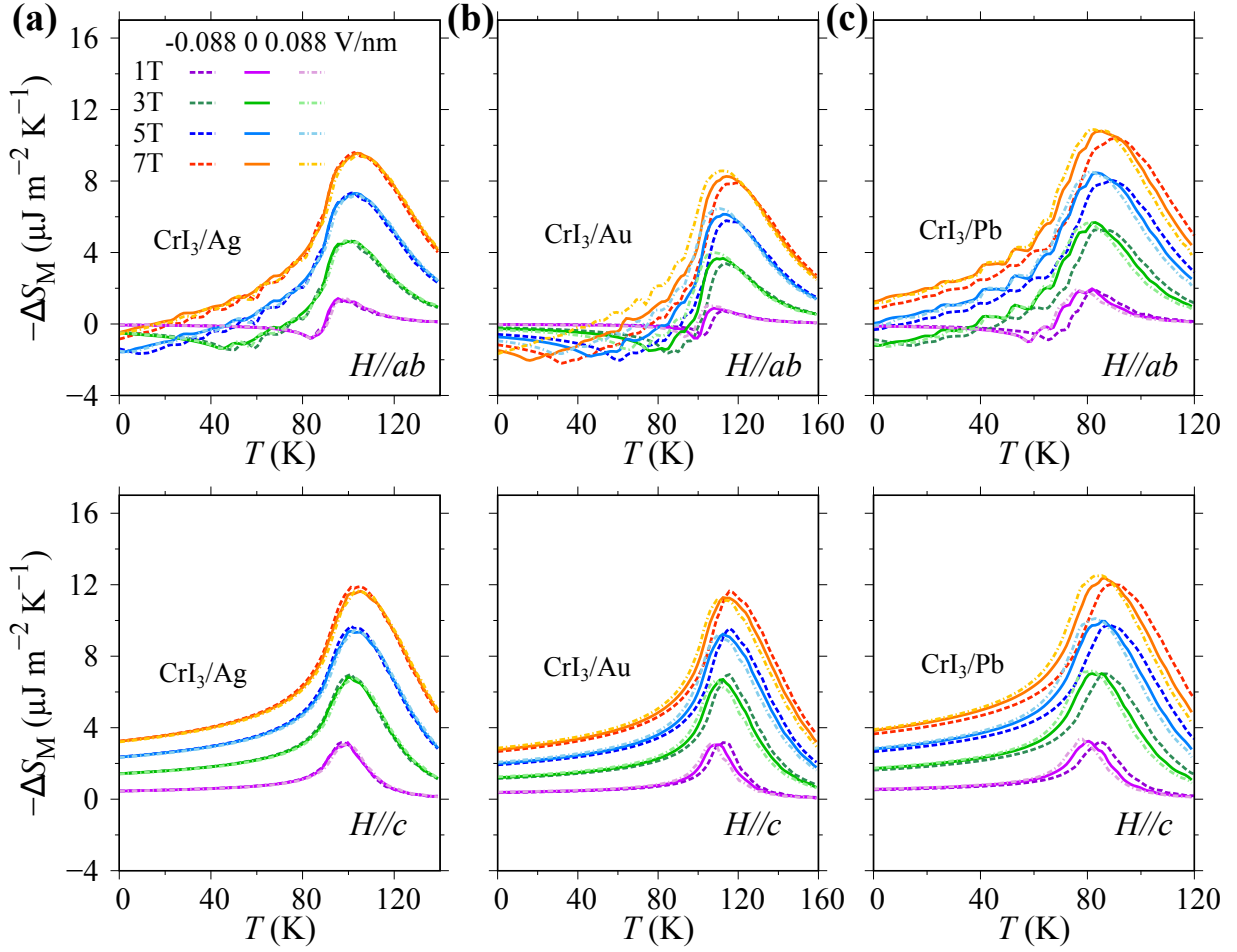


Fig. S6. Electric-field-tunable  $-\Delta S_M$  vs  $T$  curves for (a)  $\text{CrI}_3/\text{Ag}$  heterostructure, (b)  $\text{CrI}_3/\text{Au}$  heterostructure, and (c)  $\text{CrI}_3/\text{Pb}$  heterostructure with magnetic field applied in different directions (top-row subfigures:  $H//ab$ , bottom-row subfigures:  $H//c$ ).

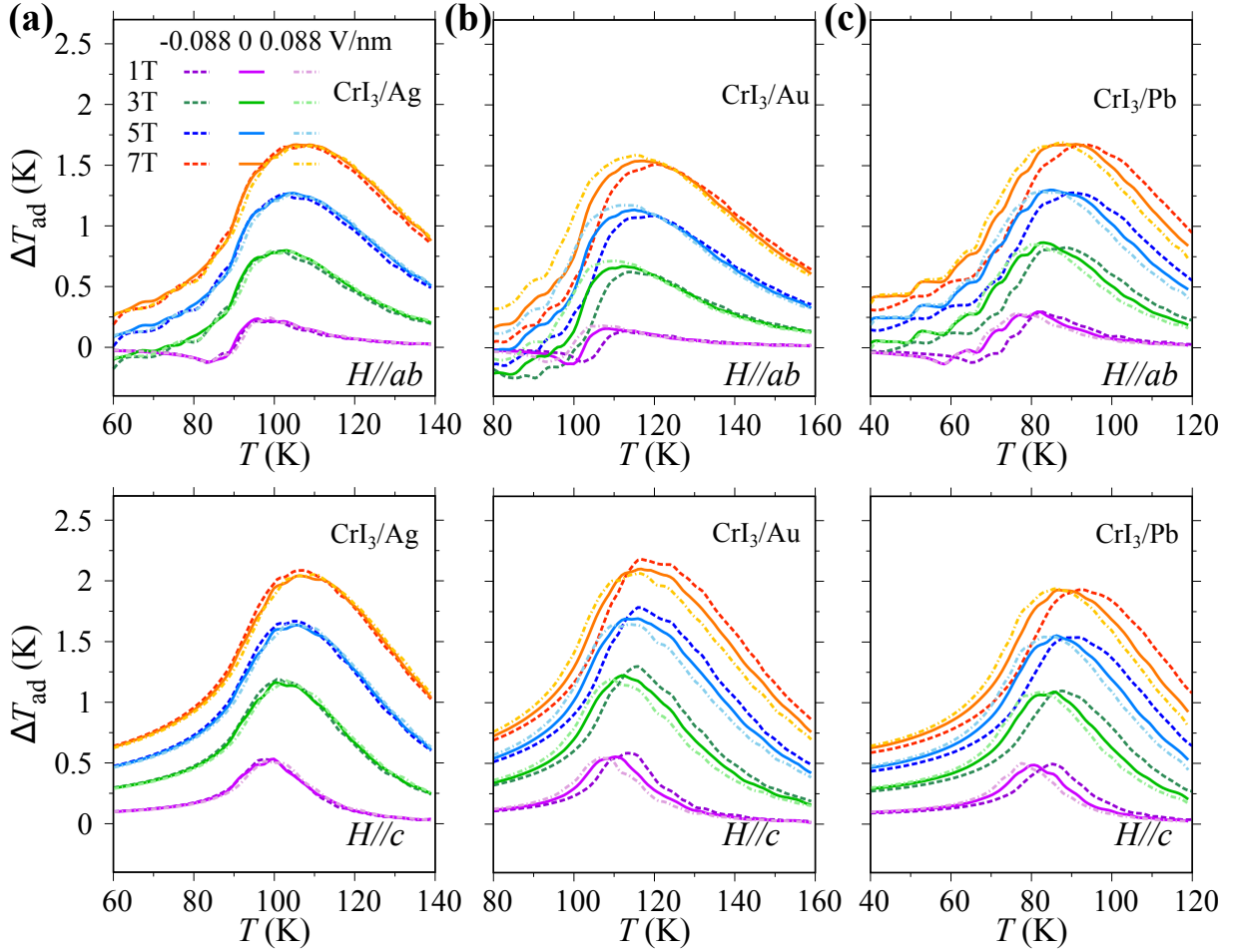


Fig. S7. Electric-field-tunable  $\Delta T_{\text{ad}}$  vs  $T$  curves for (a)  $\text{CrI}_3/\text{Ag}$  heterostructure, (b)  $\text{CrI}_3/\text{Au}$  heterostructure, and (c)  $\text{CrI}_3/\text{Pb}$  heterostructure with magnetic field applied in different directions (top-row subfigures:  $H//ab$ , bottom-row subfigures:  $H//c$ ).

## References

- (1) Li, H.; Xu, Y. K.; Lai, K.; Zhang, W. B. The enhanced ferromagnetism of single-layer  $\text{CrX}_3$  (X = Br and I) via van der Waals engineering. *Physical Chemistry Chemical Physics* **2019**, *21*, 11949–11955.